

# Anomalous emission from a one-dimensional lattice of ions in silicon photonics

Arindam Nandi<sup>2</sup>, Xiaodong Jiang<sup>2</sup>, Dongmin Pak<sup>2</sup>, Daniel Perry<sup>1</sup>, Kyunghun Han<sup>2</sup>, Edward S Bielejec<sup>1</sup>, Yi Xuan<sup>2</sup>, Mahdi Hosseini<sup>2,\*</sup>

<sup>1</sup>*Sandia National Laboratory, Albuquerque, NM 87185, USA*

<sup>2</sup>*Birck Nanotechnology Center, School of Electrical and Computer Engineering, Purdue University, West Lafayette, IN 47907, USA*

\* *mh@purdue.edu*

**Intermodal coupling between optically active quantum centers can be achieved by engineering the environment of radiative atoms enclosed by photonic structures<sup>1</sup>. The interaction between multiple modes of the system may give rise to anomalous propagation<sup>3</sup> where loss is suppressed in certain regimes. Understanding the complex mode dynamics towards engineering many-body quantum interactions has been the subject of intensive research in recent years. Here, we observe anomalous photon emission at the telecommunication wavelength from an atomic Bragg grating composed of close to 1000 atomic mirror segments. We observe an enhanced and asymmetric emission spectrum from the ions and attribute it to Borrmann-type loss suppression and Fano-type interference<sup>3</sup> of propagating modes in the system, respectively. Our observation paves the way for designing active materials and novel topological photonics<sup>3</sup> with engineered linear and nonlinear interactions for broad applications. In particular, the rich dynamics of coupled modes in the system can be used to overcome losses and thus engineer interaction Hamiltonian for future quantum photonic networks<sup>4</sup>.**

Novel phenomena emerge when resonant modes of a hybrid system undergo coherent interactions<sup>3</sup>. The interaction of this kind may result in engineering unconventional materials and platforms for broad applications. In photonics, the coherent and cooperative mode coupling has resulted in observation of peculiar effects including Fano interference<sup>3</sup>, cooperative light scattering,<sup>5,6</sup> cavity quantum electrodynamic interactions<sup>7,8</sup>, Borrmann effect<sup>9</sup>, and topological

quantum optical effect<sup>3,10,11</sup>. Compared with the laser-cooled atomic systems<sup>5,6</sup>, the controllable dynamics of mode coupling in solid-state platforms is more challenging due to the adverse environmental effects imposed by the solid host. To date, significant advancements in on-chip single photon generation based on active centers in solids and passive silicon photonic resonators<sup>12</sup> have been achieved and signatures of cooperative emission from ensembles of quantum emitters has been reported<sup>13</sup>. The relatively low sensitivity of the rare earth (RE) ions to the solid's environment makes the RE ions attractive for realization of linear and nonlinear light-matter interactions for quantum applications. The RE doped crystals have been used to show coherence times of up to 6 hours<sup>14</sup>, low inhomogeneous broadening of about 10s of MHz<sup>15</sup> (five orders of magnitude smaller than broadening observed in silicon), >70% quantum storage efficiency<sup>16</sup> and >50 GHz storage bandwidth<sup>17</sup>, and generation of indistinguishable photons by integration with silicon photonics<sup>18</sup>. Albeit RE-doped silicon photonic elements have been used for demonstration of quantum effects, the large inhomogeneous broadening and low coherence time of RE ions when embedded in silicon materials has limited the practical applications of such materials in scalable quantum photonic networks.

Here, by activation of silicon photonic structures using precision ion implantation, we control the ensemble emission through design of the atomic geometry and study collective coupling between different modes of the system. We take advantage of the inhomogeneous broadening of ions in silicon materials and the topology of the structure to design photonic materials suppressing optical loss, thus enhancing photon emission. We observe asymmetric lineshapes of photon emission governed by Fano interference between emission modes and resonator modes of the system.

We use isotopically pure <sup>168</sup>Er ions directly implanted in a SiN ring resonator into a periodic array (see Fig.1 (a)). Er ions are implanted into an ion array, separated by an integer number of the Er emission wavelength, with a precision of  $\pm 10$ nm. As the ions are separated by a distance equal to the effective wavelength of the emitted light inside the resonator, the emission is enhanced under the Bragg condition with the atomic Bragg mode coupled to the optical mode of the photonic resonator. At the Bragg condition, enhanced intra-cavity photon number is ex-

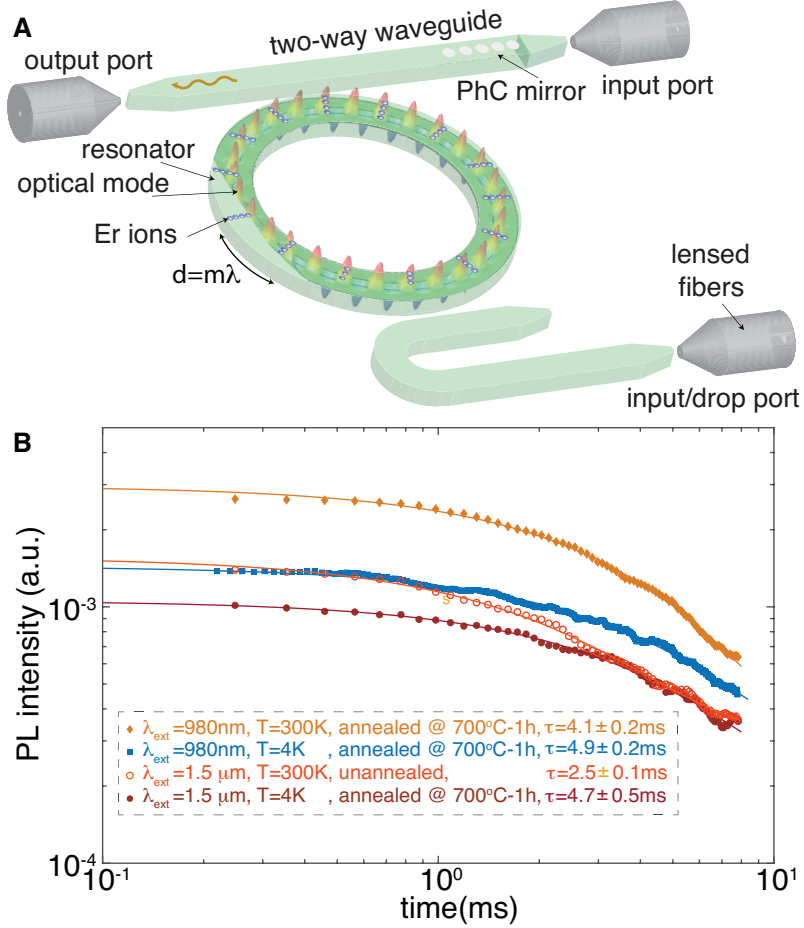


Figure 1: **Schematic of the designed active SiN ring resonator.** (a) Isotopically pure  $^{168}\text{Er}$  ions are implanted at the antinodes of the cavity separated by multiples of the wavelength of Er emission. At each segment, around  $10^4$  ions were implanted along the diameter of the ring. A photonic crystal mirror is used to increase the collection efficiency to the lensed fiber on the left (output port). The excitation pump enters the ring either from the drop-port or the mirror-side waveguide using another lensed fiber. (b) Photoluminescence decay of ions in the resonator is shown under 980nm (off-resonant) and 1.5  $\mu\text{m}$  (on-resonant) excitation of annealed and not-annealed sample. The lifetime after annealing is independent of temperature indicating negligible non-radiative decay.

pected, which is directionally emitted into the resonator waveguide. The ultimate example of such effect was given by Borrmann in 1941<sup>19</sup> describing anomalous transmission of x-ray beam through perfect crystals. In addition, the coupling between the resonating Bragg mode and the

resonator mode gives rise to Fano resonances in the system with asymmetric lineshapes.

The photoluminescence decay from the ions in a SiN resonator is plotted in Fig. 1(b) for annealed and unannealed samples (see Methods). The emission is measured using pump light at 980nm and 1.5  $\mu$ m. The lifetime is radiative limited for the annealed samples and is independent of the temperature. To obtain the resonant emission spectrum we use a pump light near 1.5 $\mu$ m that is resonant with the Er ions and the SiN resonator. After 6ms of pumping, the pump is switched off to measure the photon emitted from the ions into the ring resonator collected by a lensed fiber. The emitted mean photon number ( $\langle n \rangle_{emitted}$ ) is measured at every free-spectral range of the cavity. The resulted emission spectrum at 4K temperature is shown in Fig.2A, which significantly deviates from the emission of the ions at room temperature, with the peak measured emission near 1520 nm. We observed that the absolute photon emission at room temperature is higher by a factor of about 20 compared to 4K, an effect attributed to phonon-assisted excitation<sup>20</sup>. The emitted photon number at 1520nm relative to 1532nm is however anomalously high at 4k compared to that at room temperature. Considering a calculated effective group index of 1.58, the Bragg condition is satisfied at 1520nm when atomic lattice spacing is an integer multiple of 962nm. For measuring the emission spectrum, we test two ring resonators with the same radius and atom spacings of 4 $\times$ 962nm (ringA) and 960nm (ringB). RingA has four times less atom number (atomic segments) than ringB. The bus waveguide is designed to maximally transmit the TM polarization by tapering the waveguide at the fiber-waveguide interface. Due to the large width of the resonator, TM1 mode with effective mode index of 1.54 is efficiently coupled to the resonator with more than 60% coupling efficiency having a loaded Q factor of about  $7 \times 10^4$ . The calculated group index for this mode is about 1.58. The data in Fig2A shows the normalized probability of emission as a function of the excitation laser wavelength and is measured for ringA showing enhanced emission contrast of 1520nm compared to the emission peak around 1532 nm. As phonon-assisted excitation exist at room temperature, multiple emission lines contribute to the PL spectrum masking the Bragg effect. Therefore, the effect is only visible at low temperatures. The emission decay rate measured at different wavelengths shows negligible change around 1520 nm ruling out possibility of dominant superradiance emission from the ions (see Methods). The lengthened decay time around 1536 nm is due to enhanced reabsorption

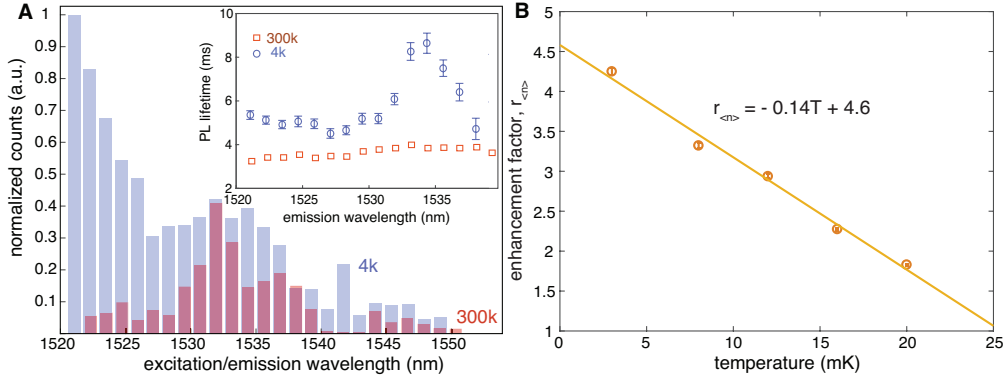


Figure 2: (A) Resonance photoluminescence spectrum at 4K (blue bars) and 300K (red bars). The enhanced emission around 1520nm is a signature of Borrmann-like enhanced emission of the ion ensemble. The inset shows the PL lifetime for 4K (blue squares) and 300K (red circles). The longer PL decay time around 1535nm is associated with enhanced reabsorption and loss of photons away from the Bragg condition. (B) The ratio ( $r_{<n>}$ ) between peak emission photon number at 1520nm to that at 1532 nm as a function of temperature. As the temperature rises, so does the phonon-assisted excitation probability. The rate of increase in phonon-assisted excitation in case of 1532nm transition is greater than that of 1520nm transition, which causes negative slope in the plot of  $r_{<n>}$  vs. temperature. The error bars in this and rest of the figures are the statistical errors and wherever not shown are smaller than the symbol size.

(loss) at the peak emission wavelength incommensurate with the atomic lattice. The intensity enhancement factor ( $r_{<n>}$ ), e.g. the ratio of the peak emission at 1520nm to emission at 1532 nm, is plotted in Fig2B as a function of the temperature. The phonon-assisted excitation is responsible for the reduction of the enhancement factor as temperature increases and asymptotes to zero at high temperatures. We were not able to measure the ratio at higher temperatures due to short-time stability of the cryostat at temperatures higher than 25K.

Figure 3A shows the total photons emitted from ions in ringA and ringB as a function of the spacing parameter,  $\zeta = d/m\lambda$ , where  $m = 1\&4$  for the two resonators, respectively. The dashed lines show the model used to describe the spectrum. The center peak ( $\zeta \sim 0.992$ ) corresponds to the typical emission around 1532 nm, which is inhomogeneously broadened. We use a Gaussian function to model the emission centered around 1532nm with an inhomogeneous width of about 2nm. The enhanced PL around  $\zeta = 1$  is associated with the Borrmann-like enhancement of the emission modeled with a beta distribution function (see Supp. Info.). The atoms centered at the anti-nodes of the resonator have a Gaussian distribution with width of around 40nm. Moreover,

the inhomogeneous broadening in the emission spectrum gives rise to exponential decrease of the photon counts around 1520nm as a function of the wavelength. In our case, the former process dominates the later, due to the extended length of the ion chain and incommensurability of the wavelength with the lattice away from the resonance. By comparing the fitted amplitudes of the Gaussian (describing PL emission around 1532nm) and Beta distribution (describing the anomalous emission around 1520nm) functions we observe nonlinear dependence of the relative emission to the atom number. In absence of the Bragg condition, the ratio between the two emission peaks (around 1520nm and 1532nm) is independent of the atom number. A quadratic dependence of emission to the atom number, or more precisely the number of atomic segments, is expected for an optically thin ensemble of atoms in the Bragg conditions<sup>6</sup>. We observe that the ratio between the anomalous and normal PL emission,  $r_{sn}$ , scales nonlinearly with the number of atomic segments. In the case of data in Fig. 3A, the resonator with  $m = 1$  has four times more atoms compared to the resonator with  $m = 4$  and assuming quadratic dependence on atom number, we ideally expect an  $r_{sn} \sim 4$ . The values extracted from the model plotted in Fig. 3A returns  $r_{sn} = 2.4 \pm 0.5$  which suggests nonlinear dependence of emission to the atom number. The deviation from the expected quadratic enhancement is due to different quality factors of ringA and ringB.

The coupling between the Bragg mode and the optical resonance mode is expected to introduce asymmetry in the emission linewidth described by Fano parameter <sup>3</sup>,  $q$ . This is evidenced by the observed lineshapes in Fig. 3B and 3C. A non-zero Fano parameter is fitted to the emission spectrum centered around 1520nm for both ringA and ringB while the emission spectrum around 1532nm is described by a symmetric Lorentzian function. To obtain this data, we collect PL from the ions after pump excitation at different frequencies around the the cavity resonance near 1520 nm and 1532 nm.

By engineering collective and long-range interactions between hybrid modes of the system, we observed anomalous emission from an ion array. Moreover, we observed mode-coupling between atomic Bragg mode and optical modes of the system. Our study paves the way for designing artificial materials with enhanced nonlinearity and controllable multimode dynamics<sup>21</sup>

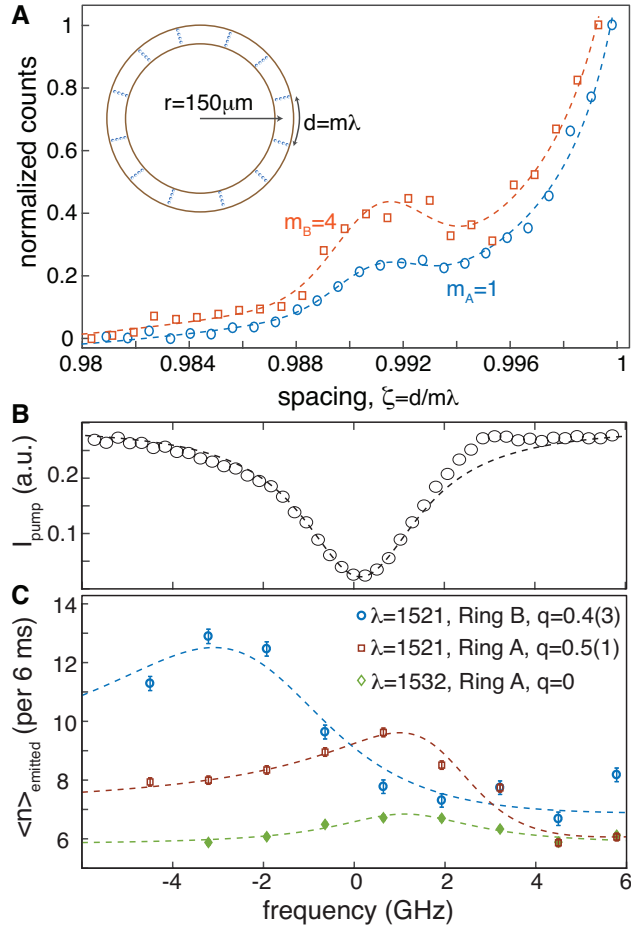


Figure 3: (A) Normalized emission (probability) as a function of spacing parameter,  $\zeta$ , for ringA (blue circles) and ringB (red circles). (B) Transmitted spectrum of the pump light through ringA with fitted Lorentzian width of  $2.6 \pm 0.1$ GHz. (C) Emission spectrum near cavity resonance at 1520 and 1532nm for ringA and ringB. The spectrum is fitted with Fano-Lorentzian lines with asymmetry described by Fano parameter (see Supp. Info.). Because the Bragg mode is almost negligible around 1532nm transition, we see a symmetric line shape at 1532nm transition.

as well as design of active topological quantum photonic structures<sup>10,11</sup>. Novel structures of this kind may be used for broad applications in sensing through octave-spanning frequency comb generation<sup>22</sup>, classical and quantum communication through on-chip lasing and single photon generation<sup>23,24</sup>, quantum photonic information processing through photon-photon interactions<sup>25</sup> and study of many-body dynamics<sup>26,27</sup>.

M.H. acknowledge funding from the Tellabs Foundation. Ion implantation was performed at Sandia National Laboratories through the Center for Integrated Nanotechnologies, an Office of Science facility operated for the DOE (contract DE-NA-0003525) by Sandia Corporation, a

Honeywell subsidiary. The views expressed here do not necessarily represent the views of the U. S. Department of Energy (DOE) or the U. S. Government.

## Methods

*Experiment setup.* The microring resonators were fabricated using a 500nm thick SiN layer on SiO<sub>2</sub>. The width and diameter of the ring is 1.5 $\mu$ m and 150 $\mu$ m, respectively (See S.I. for more details). The ion implantation of isotopically pure <sup>168</sup>Er<sup>2+</sup> ions were carried out at the Sandia National Laboratories using (see Supp. Info. for details). The energy used for the implantation was 200 keV with implantation depth of 50nm. About 10<sup>4</sup> ions were implanted in a rectangular area of width 20nm along the radius of the ring. The sample was then annealed at 1100°C for one hour in Nitrogen flow of 5.0 standard liter per minute (SLPM). A 1  $\mu$ m layer of PMMA was spin coated on the sample as an upper-cladding after annealing. The sample was placed inside a cryostat with typical temperature of 4K with two optical fibers directing light to/from the sample from/to the room-temperature setup outside the cryostat for measurement. The atoms were excited by a tunable diode laser (TLB-6700) from 1520nm to 1550nm. Typical input power of the pump in the experiments was around 5  $\mu$ W, below the saturation limit of the erbium ions. Two AOMs were used to create a pulse to pump the atoms for 6ms and turn it off for 10ms during the PL measurement. The PL light was detected using a single photon detector and counts were averaged over 10<sup>5</sup> runs.

*Atomic Bragg resonance.* The long-range emission is theoretically described using a 1D theory of atoms coupled to a resonator <sup>6</sup>. The detail of the theory is provided in the Supp. Info. In short, the probability of a single atom emitting into the resonator mode relative to other modes is given by atomic cooperativity,  $\eta$ . The photon propagates for a distance,  $z$ , experiences a phase shift of  $2\pi$  when  $z = \lambda$ . Describing the emission and propagation using transfer matrices,  $T_a$  and  $T_f$ , the total transfer matrix is given by  $M_{array} = \prod_{j=1}^{j=N} T_{a,j} \cdot T_{f,j}$ , where  $j$  refers to discrete atomic segments. The emission probability is then  $M_{array} = |M(1, 2)/M(2, 2)|^2$ . Although, the effective cooperativity averaged over atomic distribution and atomic frequency is much less than one, in our system, the bare cooperativity is around one (see Supp. Info.). The spatial arrangement of the



atoms enables observation of the long-range emission despite being in the “bad cavity” regime.

*The Borrmann effect.* The observed enhanced emission is attributed to the Borrmann effect engineered in our structure. As elegantly described in Ref.<sup>3</sup>, the Borrmann effect is visible when two oscillating modes with opposite decay rates,  $\gamma_1 = -\gamma_2$  interact under the dissipative Bragg condition. In the case of our system, the photons symmetrically emitted to the ring cavity propagating in opposite directions ( $\gamma_1 = -\gamma_2$ ) are coupled via the atoms. The nodes of the resonator mode is fixed at the position of atomic segments, where gain occurs, while the antinodes are located between the atomic segments where loss occurs. As the result, the emission mode propagates inside the cavity where loss is suppressed and eventually coupled to the bus waveguide.

*Contribution from sub- and super-radiant modes.* In presence of disorder, e.g. inhomogeneous broadening, mesoscopic cooperative decay of the symmetric and timed Dicke states<sup>28,29</sup> can still be observed as simultaneous presence of sub and superradiant modes<sup>6</sup>. The necessary condition for observation of superradiance is  $\Omega/N \ll \tau$ , where  $\Omega$  is the width of the inhomogeneous broadening,  $N$  is the total atom number,  $\tau$  is the excited state lifetime. The combination of large inhomogeneous broadening ( $\sim 300\text{GHz}$ ), limited atom number  $\sim 10^6$  and long excited state lifetime  $\sim 5\text{ms}$  suppresses the superradiant emission in our system.

*Fano interference.* Asymmetric line shape occurs when two oscillators having very different damping rates interfere, thus producing narrow spectral features<sup>3</sup>. As the phase of the strongly damped oscillator varies very slowly, and the phase changes completely (by  $\pi$ ) for the undamped oscillator at the resonance, the resulting spectra becomes asymmetric. For our system, the coupling between the Bragg mode (continuum mode) and the ring resonator (discrete mode) gives rise to asymmetric emission lines, where phase change of the Bragg mode happens very slowly compared to the ring resonator mode. The asymmetry in the lineshape is characterized by the Fano parameter  $q = \cot \delta$ , where  $\delta$  is the phase shift of the Bragg mode with respect to the cavity mode.

## Referecnes

1. Chang, D. E., Douglas, J. S., Gonzalez-Tudela, A., Hung, C. L. & Kimble, H. J. Colloquium: Quantum matter built from nanoscopic lattices of atoms and photons. *Rev. Mod. Phys.* **90** (2018).
2. Limonov, M. F., Rybin, M. V., Poddubny, A. N. & Kivshar, Y. S. Fano resonances in photonics. *Nature Photonics* **11**, 543 (2017).
3. Lu, L., Joannopoulos, J. D. & Soljacic, M. Topological photonics. *Nat. Photonics* **8**, 821–829 (2014).
4. O’Brien, J. L., Furusawa, A. & Vuckovic, J. Photonic quantum technologies. *Nat. Photonics* **3**, 687–695 (2009).
5. Goban, A. *et al.* Superradiance for atoms trapped along a photonic crystal waveguide. *Physical review letters* **115**, 063601 (2015).
6. Sørensen, H. *et al.* Coherent backscattering of light off one-dimensional atomic strings. *Physical review letters* **117**, 133604 (2016).
7. Roy, D., Wilson, C. M. & Firstenberg, O. Colloquium: Strongly interacting photons in one-dimensional continuum. *Rev. Mod. Phys.* **89** (2017).
8. Haroche, S. Nobel lecture: Controlling photons in a box and exploring the quantum to classical boundary. *Rev. Mod. Phys.* **85**, 1083–1102 (2013).
9. Novikov, V. & Murzina, T. Borrmann effect in photonic crystals. *Optics letters* **42**, 1389–1392 (2017).
10. Barik, S. *et al.* A topological quantum optics interface. *Science* **359**, 666–668 (2018).
11. Mittal, S., Goldschmidt, E. A. & Hafezi, M. A topological source of quantum light. *Nature* **561**, 502 (2018).
12. Bogdanov, S., Shalaginov, M. Y., Boltasseva, A. & Shalae, V. M. Material platforms for integrated quantum photonics. *Opt. Mater. Express* **7**, 111–132 (2017).

13. Scheibner, M. *et al.* Superradiance of quantum dots. *Nature Physics* **3**, 106 (2007).
14. Zhong, M. *et al.* Optically addressable nuclear spins in a solid with a six-hour coherence time. *Nature* **517**, 177–180 (2015).
15. Chukalina, E., Popova, M., Korableva, S. & Abdulsabirov, R. Fine structure of spectral lines in  $\text{LiF}:\text{Er}^{3+}$  due to isotopic disorder in the lattice. *Phys. Lett. A* **269**, 348–350 (2000).
16. Hedges, M., Longdell, J., Li, Y. & Sellars, M. Efficient quantum memory for light. *Nature* **465**, 1052–1056 (2010).
17. Zhong, T., Kindem, J. M., Rochman, J. & Faraon, A. Interfacing broadband photonic qubits to on-chip cavity-protected rare-earth ensembles. *Nat. Commun.* **8** (2017).
18. Dibos, M., Raha, M., Phenicie, C. M. & Thompson, J. D. Atomic source of single photons in the telecom band. *Phys. Rev. Lett.* **120** (2018).
19. Borrmann, G. Über extinktionsdiagramme der röntgenstrahlen von quarz. *Zeitschrift für Physik* **42**, 157–62 (1941).
20. Miyakawa, T. & Dexter, D. Phonon sidebands, multiphonon relaxation of excited states, and phonon-assisted energy transfer between ions in solids. *Physical Review B* **1**, 2961 (1970).
21. Staude, I. & Schilling, J. Metamaterial-inspired silicon nanophotonics. *Nature Photonics* **11**, 274 (2017).
22. Brasch, V. *et al.* Photonic chip-based optical frequency comb using soliton cherenkov radiation. *Science* **351**, 357–360 (2016).
23. Wang, Z. *et al.* Novel light source integration approaches for silicon photonics. *Laser & Photonics Reviews* **11**, 1700063 (2017).
24. St-Jean, P. *et al.* Lasing in topological edge states of a one-dimensional lattice. *Nat. Photonics* **11**, 651–656 (2017).
25. Hallett, D. *et al.* Electrical control of nonlinear quantum optics in a nano-photonic waveguide. *Optica* **5**, 644–650 (2018).

26. Dhar, H. S., Zens, M., Krimer, D. O. & Rotter, S. Variational renormalization group for dissipative spin-cavity systems: Periodic pulses of nonclassical photons from mesoscopic spin ensembles. *Phys. Rev. Lett.* **121** (2018).
27. Mazzucchi, G., Caballero-Benitez, S. F., Ivanov, D. A. & Mekhov, I. B. Quantum optical feedback control for creating strong correlations in many-body systems. *Optica* **3**, 1213–1219 (2016).
28. Dicke, R. H. Coherence in spontaneous radiation processes. *PHYS REV* **93**, 99–110 (1954).
29. Czarnik, J. W. & Fontana, P. R. Resonance radiation from interacting atoms. *J. Chem. Phys.* **50**, 4071–& (1969).
30. Shahbazyan, T. V., Raikh, M. E. & Vardeny, Z. V. Mesoscopic cooperative emission from a disordered system. *Phys. Rev. B* **61**, 13266–13276 (2000).

## Supplementary Information for:

### Anomalous emission from a one-dimensional lattice of ions in silicon photonics

Arindam Nandi<sup>†</sup>, Xiaodong Jiang<sup>†</sup>, Dongmin Pak<sup>†</sup>, Daniel Perry<sup>\*</sup>, Kyunghun Han<sup>2</sup>, Edward S Bielejec<sup>\*</sup>, Yi Xuan<sup>†</sup>, Mahdi Hosseini<sup>†</sup>

<sup>\*</sup> Sandia National Laboratory, Albuquerque, NM 87185, USA

<sup>†</sup> Birck Nanotechnology Center, School of Electrical and Computer Engineering, Purdue University, West Lafayette, IN 47907, USA

#### S.1 Theory

**Bragg condition.** The emission from the ion array is theoretically described by a 1D theory of atoms coupled to a resonator. For a single atom in the cavity, the ratio between the spontaneous emission into the cavity,  $\Gamma_{1D}$  to that of free-space,  $\Gamma$ , is given by cooperativity defined purely using geometrical factors[S1] as:  $\eta_0 = 24\mathcal{F}/\pi k^2 A$ , where  $\mathcal{F} = \nu_{FSR}/\nu_{FWHM}$  is the resonator finesse,  $\nu_{FSR}$  is the free-spectral range,  $\nu_{FWHM}$  is the resonator linewidth,  $k$  is the wavenumber, and  $A$  is the cross section of the resonator. A multilevel system, this ratio is modified by the branching ratio which in our case is about 0.21 [S2]. We calculate the bare cooperativity,  $\eta_0$  using the measured FSR, cavity linewidth and assuming 0.7% of mode energy at the ions' position and find values of approximately 1.25 and 2.25, for ringA and ringB respectively. To account for the inhomogeneous broadening, atomic distribution and lattice incommensurability we calculate the effective cooperativity of each atomic segment of width  $\delta = R d\theta$  by calculating the convolution function as :

$$\eta_j = - \int_{-\infty}^{\infty} f(\lambda) d\lambda \int_{-\lambda/2}^{\lambda/2} \eta_0/2 \cos^2[k(ja_0 + x)] \times (\tanh[j(a_0 - \lambda) - \delta/2 + x] - \tanh[j(a_0 - \lambda) + \delta/2 + x]) dx \quad (1)$$

where  $f(\lambda)$  is the frequency distribution of atomic transition due inhomogeneous broadening approximately described by a Gaussian function. In the case of current work,  $\delta \simeq 40nm$  and total number of atom segments is 245 and 980 for ringA and ringB, respectively. For simplicity, we assume a relatively flat inhomogeneous broadening distribution of atomic frequency in the

range where PL drops around  $\zeta = 1$ . The effective cooperativity averaged over all atoms can be calculated using the above equation with value less than 0.1. For a perfect point-like ion array ( $\eta_0 = \eta_j$ ) the normalized emission probability from the ensemble is given by multiplying the transfer matrix of each ion segment as:

$$P_{array} = \left| \frac{M(1, 2)}{M(1, 1)} \right|^2 \quad (2)$$

where

$$M_{array} = T_{a,N} \cdot T_{f,N} \cdot T_{a,N-1} \cdot T_{f,N-1} \dots T_{a,1} \cdot T_{f,1}. \quad (3)$$

and

$$T_{a,j} = \begin{pmatrix} 1 - \eta_j/2 & -\eta_j/2 \\ \eta_j/2 & 1 + \eta_j/2 \end{pmatrix} \quad (4)$$

$$T_{f,j} = \begin{pmatrix} e^{ika_j} & 0 \\ 0 & e^{-ika_j} \end{pmatrix} \quad (5)$$

are the transfer matrices of atomic segment  $j$  and free-space propagation from  $j - 1$  to  $j$  segment. As the excitation emission wavelength deviates from the lattice spacing, it becomes incommensurate with the lattice and therefore the emission drops. Figure S4 shows a plot of  $P_{array}$  for  $\eta_0 = 0.25, 1.25$  and  $2.5$ . At bare cooperativities close or higher than one, the probability decays approximately as a beta function. Therefore, in Fig. 4 of the main text, we used a beta function to fit the initial drop in the emission probability.

**Fano interference.** The interference between a discrete quantum state and a continuum band of states gives rise to Fano resonances. The shape of the resonant spectrum can be represented by the Fano Formula [S3]:

$$\sigma(E) = D^2 \frac{(q + \Omega)^2}{1 + \Omega^2}$$

where  $E$  denotes the energy,  $q = \cot \Delta$  is the Fano Parameter,  $\Delta$  is the phase shift of the continuum,  $\Omega = 2(\omega - \omega_0)/\Delta\omega$ , where  $\omega_0$  and  $\Delta\omega$  are the resonance energy and width respectively, and  $D^2 = 4 \sin^2 \Delta$ . We use the above equation to fit the emission spectrum in Fig. 3C and extract the  $q$  parameter.

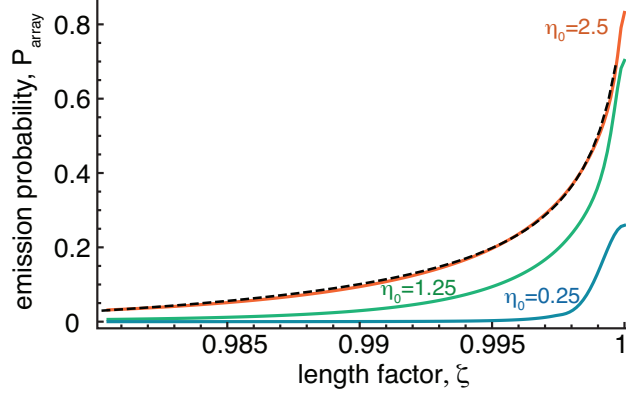


Figure S4: Emission probability plotted using Eq.2 for  $\eta_0 = 0.25, 1.25$  and  $2.5$  (solid lines). The dashed line shows the Beta probability function approximately describing the decay of the probability at high cooperativities.

\* Sub and superradiant modes

The number of Erbium ions implanted in our sample is in total about  $\sim 10^7$  for ringA. Considering yield factor of 0.1, around  $10^6$  ions will emit upon excitation. Now, the inhomogeneous broadening ( $\Omega$ ) is around 300 GHz for Er atoms in silicon around 1520nm. In our system, the cavity will work as filter to allow only a fraction of Er atoms to have a strong coupling to the incoming field. For example, as our cavity linewidth ( $\kappa$ ) is  $\sim 3$  GHz, only those Er atoms whose resonance frequency lies within that range, will interact strongly to the field and the effective  $\Omega$  can be reduced by  $\sim 100$  times. On the other hand, the effective Erbium ions interacting to the emission mode in the cavity is also reduced by the same factor as the result of the inhomogeneous broadening, making the total number of ions  $N_{eff} \sim 10^4$ .

The superradiance regime is reached in the bad cavity limit:  $\kappa \gg \gamma_{\perp}/2$ , where  $\gamma_{\perp} = 1/\tau + 1/T_2 \sim 1/T_2$ , where  $\tau$  is the single-atom lifetime of the excited state and  $1/T_2$  parameterizes additional atomic dephasing mechanisms. Another necessary condition to observe superradiance is  $\Omega/N_{eff} < \tau^{-1}$ . The last condition to satisfy is  $1/T_2 \ll g^2 N_{eff}/\kappa$  or  $\tau/T_2 \ll N_{eff}\eta$ . Taking into account the experimental parameters namely  $T_2$  of few ns [S4],  $N_{eff} \sim 10^4$  and  $\eta \sim 1$ , our system does not lie in the superradiance regime. At higher atom number, a regime of mesoscopic cooperative emission can be reached where both sub and superradiance modes are present[S5,6].

## S.2 Experimental details

The experimental setup is shown in Fig.S5A. The fabrication process of the SiN structures (Fig.S5B) starts with a (100) silicon wafer with 3  $\mu\text{m}$  thermally grown oxide layer. First, stoichiometric SiN layer of 500 nm is deposited in the horizontal tube furnace of a low-pressure chemical vapor deposition (LPCVD) tool from a gas mixture of dichlorosilane and ammonia at a temperature of 800 °C. Next, an electron-beam resist of hydrogen silsesquioxane (HSQ) is spun over the sample and device patterns. The device patterns( micro-resonator structures) are written by a 100kV ultra-high resolution, wide-field electron beam lithography (EBL) tool. Reactive-ion-etching (RIE) is then performed to etch the SiN using HSQ as an etch mask by an inductively-coupled plasma RIE machine. We use  $\text{CF}_4/\text{O}_2$  chemistry to etch the SiN to create almost vertical etching profile (Fig.S5A Inset). This method enables fabrication of high-Q ( $\sim 10^7$ ) microring resonators at 1550 nm [S7].

In order to efficiently couple light to the waveguide we use a tapered waveguide and couple the light directly from the fiber to the optical resonators. To have a stable and low-loss fiber to chip coupling for optical measurements we use patterned substrates with U-grooves (Fig.S5B) that allow self-alignment of the optical fibers to the waveguides without any active positioning of the fibers. The grooves can be placed in any orientation of the wafer using RIE dry etching, a procedure first implemented at Purdue. This method avoids limitation of the wet etching that requires devices to be precisely aligned to the crystal lattice of the wafer. The cross-section of the U-groove shows vertical and smooth sidewall profiles, defined by the Bosch process. The height of the U-groove is about 65  $\mu\text{m}$  from the bottom to the nitride layer. It is about half of the diameter of an optical fiber with cladding. Hence, by simply placing the fiber down into the groove, it allows the fiber core to be aligned with the waveguide in close proximity. Then fine tuning of the fiber position can be achieved by slight adjustment of the fiber position using the nanopositioning stages inside the cryostat.

To implant isotopically pure Er ions, we use the Sandia National Lab’s nanoImplanter (nI), which is a focused ion beam system with the ability to implant many different ion species with 10 of nm’s spot size. We first carry out mass spectrometry using a AuSiEr source before the im-



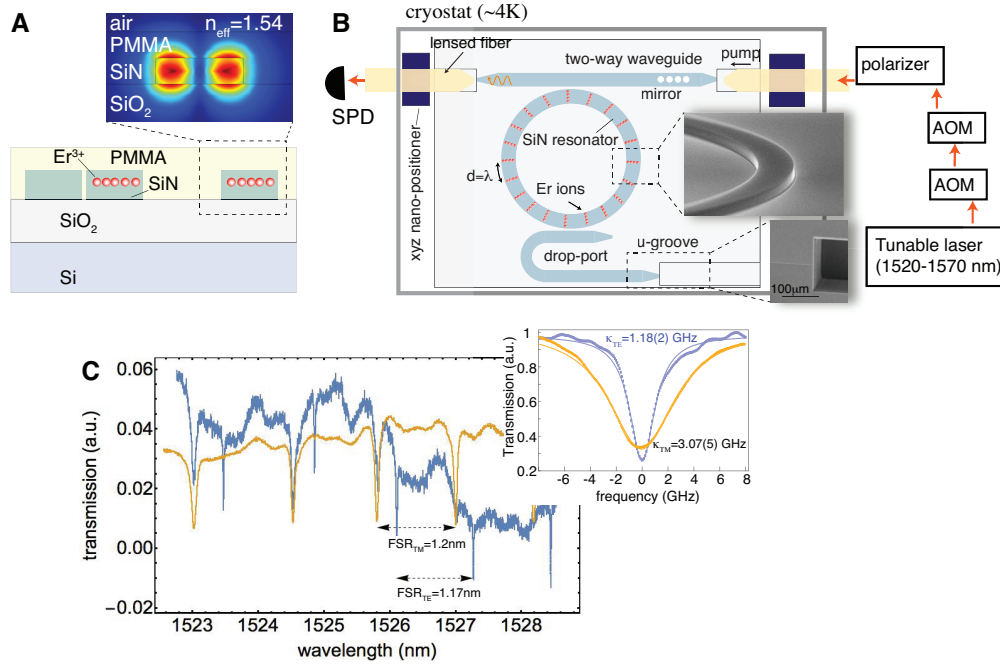


Figure S5: (A) Schematic cross section of the SiN resonator with Comsol simulation of the mode with effective index 1.58 shown in the inset. (B) Experimental setup showing two lensed fiber precisely controlled inside the cryostat using nanopositioners to couple light in and out of the sample. Inset shows the SEM images of the ring resonator wall with smooth etching and u-grooved for fiber-to-chip coupling. (C) Measured cavity transmission for the two orthogonal polarization. As the waveguide and ring are design for the TM mode, TM has the highest coupling while TE has the highest Q factor. The free-spectral range (FSR) of the two TM and TE modes and effective mode indices match the COMSOL calculations. The inset shows the fitted Lorentzian cavity transmission for TE (blue) and TM (orange) modes.

plantation and select a specific Er isotope using a combination of electric and magnetic fields (see Fig.S6). We were able to unambiguously distinguish Er<sup>+</sup>, Er<sup>++</sup> and Er<sup>+++</sup> ions as well as individual Er isotopes of 164, 166, 168 and 170. We chose <sup>168</sup>Er isotope and carried out implantation using at 200 keV Er<sup>++</sup> (100 kV accelerating voltage) and ion fluence of 10<sup>14</sup> ions/cm<sup>-3</sup>. The purity of Er isotope is about 90% based on Fig.S6 data.

We measured the dependence of the input laser power to the emission of erbium ions implanted in the ring at 4K to identify the saturation limit of the atoms. As seen from Fig.S7, the 1520nm transition saturates quicker than 1532nm transition. To avoid the saturation, we operate in the region ( 4μW) where the emission is linear with the pump power and normalize the

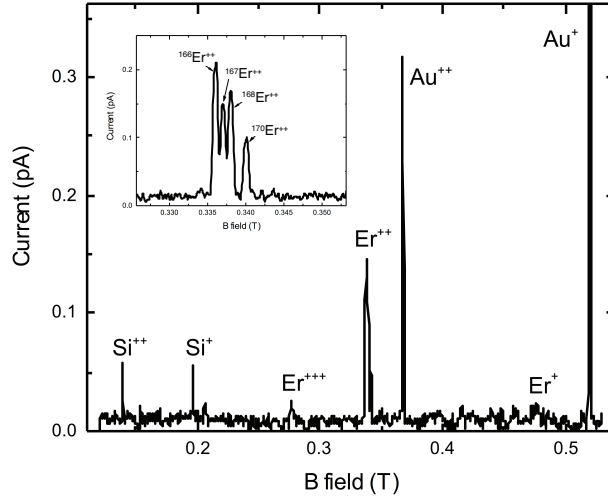


Figure S6: Mass spectrum of Er isotopes (inset) and Er, Au and Si ions measured at Sandia to deterministically select an Er isotope prior to implantation.

emission to the incident pump power.

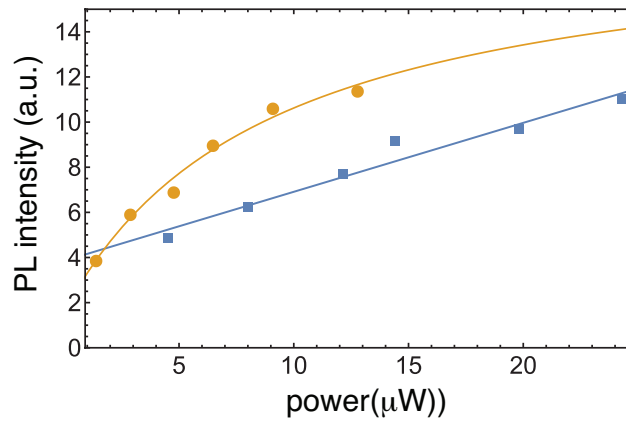


Figure S7: The dependence of the input laser power to the emission of erbium ions implanted in the ring at 4K for 1520nm and 1532nm transitions.

The room temperature data in Fig.S8 provides another evidence of phonon-assisted excitation for 1532nm transition at room temperature. The fitted FWHM of the cavity resonance measured on transmission at 1532nm is  $2.8 \pm 0.6$  GHz while the FWHM of the Erbium emission for that wavelength is  $7.3 \pm 0.6$  GHz. The emission is measured by varying the excitation wavelength around the cavity resonance and collecting emitted photons after the pump is switched off. The broadening of emission spectrum suggests phonon-assisted excitation at room temperature.

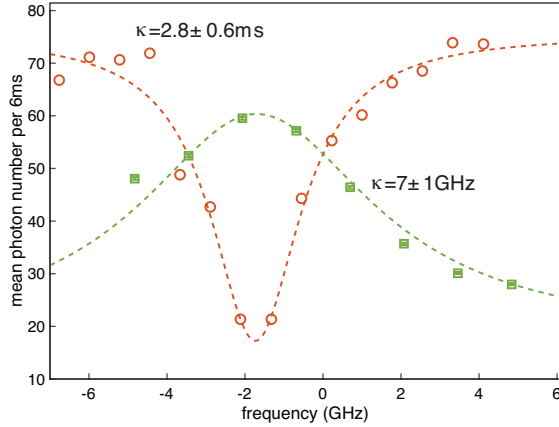


Figure S8: Emission spectrum (green square) and pump transmission spectrum (red circle) at room temperature near 1532nm transition.

- [S1] Tanji-Suzuki, H. *et al.* Interaction between atomic ensembles and optical resonators: classical description. In *Advances in atomic, molecular, and optical physics*, vol. 60, 201–237 (Elsevier, 2011).
- [S2] McAuslan, D. L., Longdell, J. J. & Sellars, M. J. Strong-coupling cavity qed using rare-earth-metal-ion dopants in monolithic resonators: What you can do with a weak oscillator. *Phys. Rev. A* **80** (2009).
- [S3] Limonov, M. F., Rybin, M. V., Poddubny, A. N. & Kivshar, Y. S. Fano resonances in photonics. *Nature Photonics* **11**, 543 (2017).
- [S4] Staudt, M. U. *et al.* Investigations of optical coherence properties in an erbium-doped silicate fiber for quantum state storage. *Opt. Commun.* **266**, 720–726 (2006).
- [S5] Feng, W., Li, Y. & Zhu, S.-Y. Effect of atomic distribution on cooperative spontaneous emission. *Phys. Rev. A* **89** (2014).
- [S6] Shahbazyan, T. V., Raikh, M. E. & Vardeny, Z. V. Mesoscopic cooperative emission from a disordered system. *Phys. Rev. B* **61**, 13266–13276 (2000).
- [S7] Xuan, Y. *et al.* High-q silicon nitride microresonators exhibiting low-power frequency comb initiation. *Optica* **3**, 1171–1180 (2016).